Pressure-induced superconductivity in a three-dimensional topological material $ZrTe_5$

Yonghui Zhou[a,b,1], Juefei Wu[c,1], Wei Ning[a], Nana Li[d], Yongping Du[c], Xuliang Chen[a,b], Ranran Zhang[a], Zhenhua Chi[b], Xuefei Wang[b], Xiangde Zhu[a], Pengchao Lu[c], Cheng Ji[e], Xiangang Wan[c,f], Zhaorong Yang[a,b,f,2], Jian Sun[c,f,2], Wenge Yang[d,e,2], Mingliang Tian[a,f,g,2], Yuheng Zhang[a,f], and Ho-kwang Mao[d,h,2]

[a]High Magnetic Field Laboratory, Chinese Academy of Sciences, Hefei 230031, China; [b]Key Laboratory of Materials Physics, Institute of Solid State Physics, Chinese Academy of Sciences, Hefei 230031, China; [c]National Laboratory of Solid State Microstructures, School of Physics, Nanjing University, Nanjing 210093, China; [d]Center for High Pressure Science and Technology Advanced Research, Shanghai 201203, China; [e]High Pressure Synergetic Consortium, Geophysical Laboratory, Carnegie Institution of Washington, Argonne, IL 60439; [f]Collaborative Innovation Center of Advanced Microstructures, Nanjing University, Nanjing 210093, China; [g]Hefei Science Center, Chinese Academy of Sciences, Hefei 230031, China; and [h]Geophysical Laboratory, Carnegie Institution of Washington, Washington, DC 20015

Contributed by Ho-kwang Mao, January 25, 2016 (sent for review December 5, 2015; reviewed by Alexander G. Gavriliuk and Zhili Xiao)

As a new type of topological materials, $ZrTe_5$ shows many exotic properties under extreme conditions. Using resistance and *ac* magnetic susceptibility measurements under high pressure, while the resistance anomaly near 128 K is completely suppressed at 6.2 GPa, a fully superconducting transition emerges. The superconducting transition temperature T_c increases with applied pressure, and reaches a maximum of 4.0 K at 14.6 GPa, followed by a slight drop but remaining almost constant value up to 68.5 GPa. At pressures above 21.2 GPa, a second superconducting phase with the maximum T_c of about 6.0 K appears and coexists with the original one to the maximum pressure studied in this work. In situ high-pressure synchrotron X-ray diffraction and Raman spectroscopy combined with theoretical calculations indicate the observed two-stage superconducting behavior is correlated to the structural phase transition from ambient *Cmcm* phase to high-pressure *C*2/*m* phase around 6 GPa, and to a mixture of two high-pressure phases of *C*2/*m* and *P*-1 above 20 GPa. The combination of structure, transport measurement, and theoretical calculations enable a complete understanding of the emerging exotic properties in 3D topological materials under extreme environments.

high pressure | Dirac semimetals | superconductivity | synchrotron X-ray diffraction

Since the first report of topological insulator, an extensive attention in recent years has been focused on newly emergent Dirac materials including topological insulators (1–3), Dirac semimetals (4, 5), and Weyl semimetals (5–7) for their unique quantum phenomena. $ZrTe_5$ has been studied for a long time due to its large thermoelectric power (8, 9), resistivity anomaly (10, 11), and large positive magnetoresistance (12). Recent theoretical works (13, 14) have proposed that single-layer $ZrTe_5$ is a large gap quantum spin hall insulator, but the bulk $ZrTe_5$ behaves between the strong and weak topological insulator. These predictions spark the renewed interest in the investigation of its Dirac and topological characters. Indeed, the magneto-transport experiments (15) have observed the chiral magnetic effect, both angle-resolved photoemission spectroscopy (15) and magneto-infrared spectroscopy (16, 17) study show the electronic structure of $ZrTe_5$ is similar with other three-dimensional (3D) Dirac semimetals like Na_3Bi (18–20) and Cd_3As_2 (21–25). These results suggest that $ZrTe_5$ is a very promising system that hosts topological properties and might help to pave a new way for further experimental studies of topological phase transitions.

As one of the fundamental state parameters, high pressure is an effective, clean way to tune lattice as well as electronic states, especially in quantum states (26–28). In this work, by performing resistance and *ac* magnetic susceptibility measurements on $ZrTe_5$ single crystal at various pressures up to 68.5 GPa, a superconducting transition at 1.8 K was first noticed at a pressure of 6.2 GPa. It was interesting to notice that the occurrence of the metallic phase/or superconductivity at 6.2 GPa is accompanied by the complete suppression of the large resistance peak near 128 K by the pressure. Two superconducting phases were observed. One of them shows a sharp resistance drop with a zero resistance near 3.8 K, which is robust to pressure up to 68.5 GPa. The second one presents a broad resistance drop but with a finite resistance starting from 6.0 K only exists at a pressure above 21.2 GPa. In situ high-pressure synchrotron X-ray diffraction and Raman spectroscopy, combined with theoretical calculations, confirm these two pressure-induced superconducting phases correspond to the pressure-induced structural transition of $ZrTe_5$ crystal.

Results

Pressure-Induced Superconductivity. The crystals show a thin elongated rectangular shape, where the prismatic $ZrTe_6$ chains run along the crystallographic *a* axis and linked along the *c* axis via zig-zag chains of Te atoms to form two-dimensional (2D) layers, stacked along the *b* axis into a crystal (29). The freshly cleaved crystal was pressurized along the *b* axis and the standard four-probe resistance measurement was performed along the *a* axis, as illustrated schematically in Fig. 1*A*, Inset.

Fig. 1 *A* and *C* shows the evolution of electrical resistance as a function of temperature for $ZrTe_5$ single crystal at various pressures in run 1. Upon cooling at 0.5 GPa from 300 K down to 1.8 K, the overall behavior of resistance displays a typical

Significance

Three-dimensional (3D) Dirac semimetals have attracted a lot of advanced research recently on many exotic properties and their association with crystalline and electronic structures under extreme conditions. As one of the fundamental state parameters, high pressure is an effective, clean way to tune lattice as well as electronic states, especially in quantum states, thus their electronic and magnetic properties. In this paper, by combining multiple experimental probes (synchrotron X-ray diffraction, low-temperature transport under magnetic field) and theoretical investigations, we discover the pressure-induced 3D Dirac semimetal to superconductor transition in $ZrTe_5$.

Author contributions: Z.Y., J.S., W.Y., M.T., and H.-k.M. designed research; Y. Zhou, J.W., W.N., N.L., Y.D., X.C., R.Z., Z.C., X. Wang, X.Z., P.L., and C.J. performed research; X. Wan, Z.Y., J.S., W.Y., M.T., Y. Zhang, and H.-k.M. analyzed data; and Y. Zhou, Z.Y., J.S., W.Y., and M.T. wrote the paper.

Reviewers: A.G.G., Institute for Nuclear Research; and Z.X., Northern Illinois University.

The authors declare no conflict of interest.

[1]Y. Zhou and J.W. contributed equally to this work.

[2]To whom correspondence may be addressed. Email: zryang@issp.ac.cn, jiansun@nju.edu.cn, yangwg@hpstar.ac.cn, tianml@hmfl.ac.cn, or hmao@carnegiescience.edu.

This article contains supporting information online at www.pnas.org/lookup/suppl/doi:10.1073/pnas.1601262113/-/DCSupplemental.

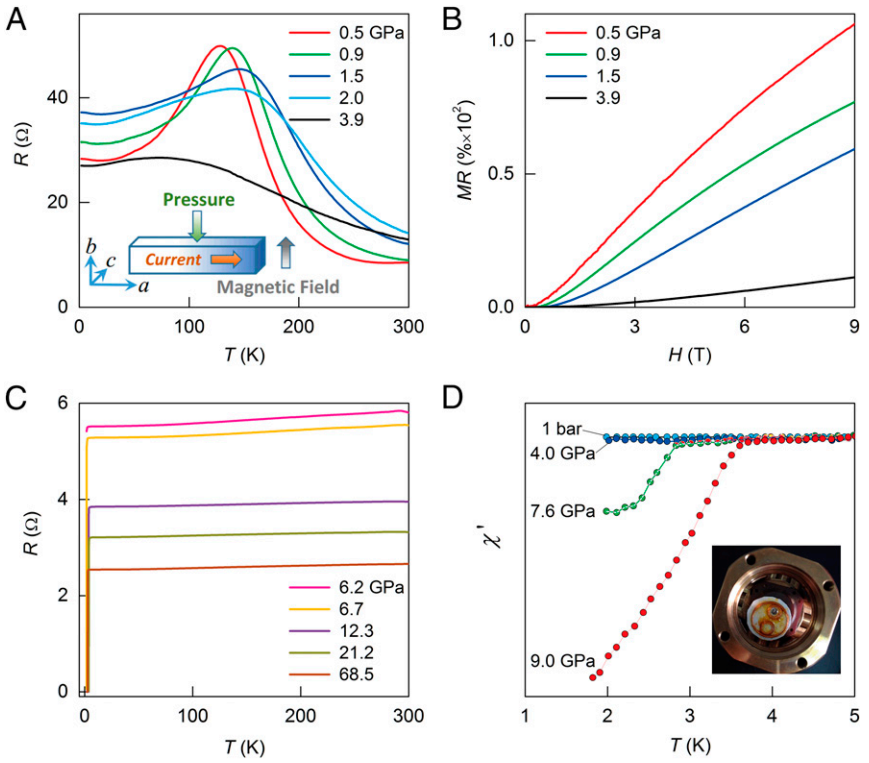

Fig. 1. Experimental evidence of pressure-induced superconductivity in $ZrTe_5$ single crystal. (*A*) Temperature-dependent electrical resistance $R(T)$ at various pressures up to 3.9 GPa. *Inset* schematically shows the arrangements of pressure, magnetic field and current applied. (*B*) Magnetoresistance (MR) measured at the peak temperature of electrical resistance anomaly. The MR is strongly suppressed with increasing pressure. (*C*) The emergence of pressure-induced superconducting transition at higher pressures ranging from 6.2 to 68.5 GPa. (*D*) The real part of the *ac* magnetic susceptibility as a function of temperature at different pressures up to 9.0 GPa. *Inset* shows the image of experimental setup for the *ac* magnetic susceptibility measurements.

semiconducting-like feature above 128 K, then the resistance decreases with the decrease of temperature followed by a slight upturn below 20 K. The large resistance anomaly around 128 K is quite similar to those observed under ambient pressure (12, 15, 30), and was generally correlated to the sign change of charge carriers although the origin still remains elusive (30). With increasing pressure, the peak temperature increases initially up to 150 K and then shifts back toward lower temperatures accompanied by the broadening of the peak and the decrease of the peak resistance. Because it was reported that the resistance anomaly could be strongly enhanced by an application of a magnetic field at ambient pressure, we investigated the magnetoresistance (MR) at the peak temperature under different pressures. As shown in Fig. 1*B*, the magnetotransport properties at each pressure show positive MR behavior with the increase of magnetic field but the magnitude of the MR decreases monotonically with the increase of pressure no matter where the peak temperature locates.

Surprisingly, with further increasing pressure, accompanied by the complete suppression of the resistance anomaly peak, a metallic transport behavior with an almost constant normal state resistance within 5% is obtained and a small drop of resistance is observed at ∼2.5 K and 6.2 GPa. At 6.7 GPa, the resistance drops to zero at 1.8 K, indicative of the appearance of superconductivity (Fig. 1*C*). To make sure that the drop of the resistance was indeed a superconducting transition, we carried out *ac* magnetic susceptibility measurements on $ZrTe_5$ at several pressures up to 9.0 GPa. As seen from Fig. 1*D*, diamagnetic signal is observed at 7.6 and 9.0 GPa, which is in agreement with the resistance results.

Fig. 2 *A* and *D* shows the blow-up of the *R*–*T* curves at different pressures near the superconducting transition. It was clearly seen that the superconducting transition is quite sharp at pressures between 8.3 and 21.2 GPa, indicating the bulk superconductivity. However, when the pressure is applied up to 30.0 GPa, the onset temperature of the resistance drop occurs from ∼6.0 K, accompanied by a gradual decrease of resistance down to 3.9 K, at which the sharp drop of resistance to zero presents, as shown in Fig. 2*D*. In fact, such a two-step-like transition can be recognized from 25.3 GPa, implying two superconducting phases coexist in the sample. With further increasing pressure, the higher superconducting phase (SC-II) is suppressed gradually but the lower one (SC-I) still survives and remains sharp feature. Clearly, the SC-I exists in a broad pressure regime from 6.2 GPa to the maximum pressure 68.5 GPa achieved in this work, and the SC-II manifests only at pressures above 21.2 GPa. To eliminate the possible pressure gradient and internal strain effect on the resistance measurements, we have repeated the experiment using Daphne 7373 oil as the pressure-transmitting medium, and observed the appearance of SC-II at same pressure range (Fig. S1).

Determination of Upper Critical Magnetic Field. Fig. 2 *B* and *E* displays temperature dependence of resistance under external magnetic fields aligned along *b* axis of $ZrTe_5$ at 14.6 and 30.0 GPa, respectively. For both cases, a finite resistive tail at low temperatures was clearly seen and gradually lifted with the increase of magnetic field. A magnetic field of 1.5 T almost erases the superconducting transition completely. By defining T_c with resistance criterion of $R_{cri} = 90\%R_n$ (R_n is the normal state resistance), we constructed the temperature (T)–magnetic field (H) phase diagrams, as shown in Fig. 2 *C* and *F*. For $P = 14.6$ GPa, T_c decreases monotonically with increasing magnetic field. The upper critical field $\mu_0 H_{c2}(0)$ is estimated to be about 1.54 T according to the Werthamer–Helfand–Hohenberg (WHH) equation (31). However, for $P = 30.0$ GPa, being associated with the

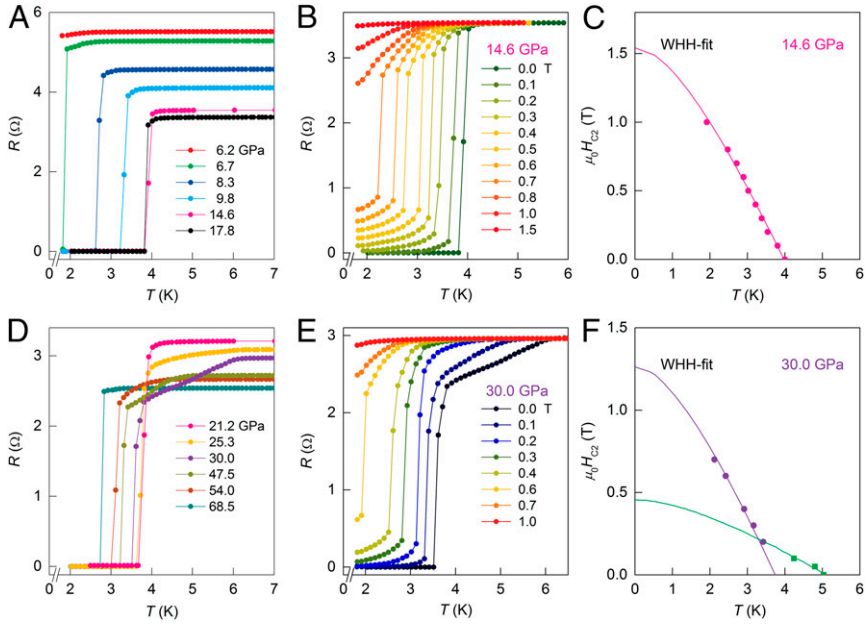

Fig. 2. Temperature-dependent resistance around superconducting transition temperatures and determination of the upper critical field for the superconducting $ZrTe_5$. (*A*) The first sharp resistance drop can be seen as the manifestation of superconductivity at 6.7 GPa. With increasing pressure, the T_c increases monotonously toward 17.8 GPa. (*D*) Above 21.2 GPa, a much higher transition emerges at around 6.0 K, suggesting a second superconducting phase. *B* and *E* show the temperature dependence of resistance under different magnetic fields parallel to the *b* axis up to 1.5 T at 14.6 GPa and up to 1.0 T at 30.0 GPa, respectively. *C* and *F* show the temperature dependence of the upper critical field $\mu_0 H_{c2}$ at 14.6 and 30.0 GPa, respectively. Here, T_c at different magnetic field is determined as 90% drop of the normal state resistance. The solid lines represent the fitting lines based on the WHH formula.

coexistence of SC-I and SC-II, the *T*–*H* phase diagram is clearly divided into two parts. The T_c is depressed more pronouncedly at fields below 0.2 T, indicating that the SC-II is sensitive to the magnetic field. At fields above 0.2 T, the superconductivity is dominated by SC-I, where the *R*–*T* curves are similar to those measured at 14.6 GPa. The T_c–*H* relationship can be described with the WHH equation both at fields below and above 0.2 T, which yields $\mu_0 H_{c2}(0)$ value of 0.46 T for SC-II and 1.26 T for SC-I. The large difference of $\mu_0 H_{c2}(0)$ indicates that the SC-I and SC-II might have different origins.

Pressure-Superconducting Phase Diagram. All of the characteristic parameters (*T* and *P*) are summarized in a *T*–*P* phase diagram shown in Fig. 3. It can be seen that, with increasing pressure, the peak temperature of the resistance anomaly initially increases up to 150 K and then decreases abruptly. When the peak anomaly disappears at the critical pressure of 6.2 GPa, superconducting phase emerges immediately, indicating a possible quantum critical point near 6.2 GPa, below which the sample is semimetal with topological character. Furthermore, if we carefully check the pressure-dependent normal state resistance at 300 and 10 K (Fig. 3, *Inset*), both pressure-induced variations of R_n intuitively follow the *T*–*P* phase diagram. The slight enhancement of the normal state resistance by the application of pressure up to 2.0 GPa is probably an indication of the pressure-induced competition of the multiband carriers of the sample.

With further increasing pressure above 6.2 GPa, T_c increases monotonically until it reaches a maximum of 4.0 K at 14.6 GPa for the SC-I. The SC-II emerges only above 21.2 GPa with the highest T_c of about 6.0 K. As shown in Fig. S1, this T_c value is also captured in run 2, confirming the appearance of SC-II phase, whereas one electrode cracked during cooling process at 25.6 GPa. It seems clear that the pressure-induced SC-I is a bulk superconductor, and the SC-II without zero resistance is not. There are a number of possibilities that may be responsible for this tiny resistance drop near 6.0 K. One of them is from the impurity or defect phase in the sample. Because the resistance drop reaches about 20%R_n, the impurity is almost unlikely in our single crystal sample but the pressure-induced disordering cannot be excluded. The second possibility is due to the occurrence of

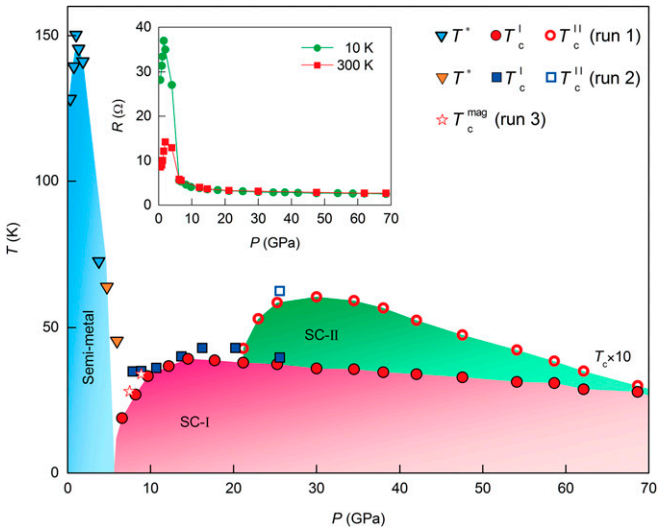

Fig. 3. Temperature–pressure phase diagram of $ZrTe_5$ single crystal. The triangle symbols denote *T**, the peak temperature of electrical resistance anomaly. The circles and squares represent T_c values extracted from electrical resistance measurements in run 1 and run 2, respectively. The pentagrams represent the onset temperature of Meissner effect in the *ac* magnetic susceptibility measurements in run 3. Colored areas are guides to the eyes indicating the distinct phases. The red region corresponds to SC-I phase where T_c is defined as 50% drop of the normal state resistance, and the green region corresponds to SC-II phase where the T_c is determined as the onset temperature of electrical resistance drop. For clarity, the value of T_c here is amplified by a factor of 10. *Inset* shows the specific resistance as a function of applied pressure at 10 and 300 K, respectively.

surface superconductivity associated with the topological surface state, because similar two-step-like transition behavior has also been reported in putative topological superconductor half-Heuslers (32). Unfortunately, the surface state of $ZrTe_5$ has not been verified yet. The third possible origin is that it is an independent superconducting phase induced by the pressure, but this phase is metastable and coexists with SC-I with different structures.

The Theoretical Calculations on the Electronic Bands and Possible Crystal Structures. To have a comprehensive understanding of the pressure-induced variations of physical properties of $ZrTe_5$, we also performed the density functional theory calculations for the electronic band structures (Fig. S2). Our results agree well with the previous study (13). To get more insights on the high-pressure phases of $ZrTe_5$, we applied the crystal structure prediction techniques to search the possible high pressure candidates under pressure up to 40 GPa. The enthalpy–pressure (ΔH–P) curves plotted in Fig. 4 show the best candidates from our structural prediction. The *Cmcm* structure is the most stable one at ambient condition, which is in agreement with the experiments. Upon compression, we find that a layered *C*2/*m* structure (denoted as *C*2/*m*-1) has the lowest enthalpy between 5 and 20 GPa, although an alloy *P*-1 structure takes the lowest entropy phases beyond 20 GPa, concurrent with the two-stage superconducting behavior under similar pressure range. The crystal structures of *C*/2*m* and *P*-1 are plotted in Fig. 4 *B* and *C*. The lattice constants and atomic positions of all the interested candidates from the theoretical crystal structure prediction are listed in Table S1.

Structure Determination with in situ High-Pressure Synchrotron X-Ray Diffraction and Raman Spectroscopy. To confirm the structure stability and the predicted new phases, we have conducted in situ high-pressure synchrotron X-ray diffraction study on the $ZrTe_5$ sample up to 55 GPa. Angle-dispersive X-ray diffraction experiments were performed on powder $ZrTe_5$ sample at room temperature. A sample chamber in the rhenium gasket preindented to 40-μm thickness followed by drilling a 100-μm hole in the center was filled with powder sample, ruby ball, and pressure-transmitting medium for in situ high-pressure study. The series powder diffraction patterns are shown in Fig. 5*A*. It is clear to see the structural transitions as pressure increases. Using the General Structure Analysis System (GSAS) software package for structure refinement (33), the corresponding phases and unit cell volumes fitted by the third-order Birch–Murnaghan equation of state (34) are displayed in Fig. 5*B*. From these XRD data, it is clear that two structural transitions occurred around 6.0 GPa and above 30 GPa, accompanied with the unit-cell volume drops of ~4.4% and ~4.8% at these phase transition critical pressures. Rietveld refinements of the high-pressure XRD patterns with known and predicted structures at these typical pressure points are shown in Fig. S3. The Bragg peaks in the experimental patterns can be well indexed by the orthorhombic phase (space group *Cmcm*) around ambient pressure and a layered monoclinic phase (*C*2/*m*) for the pattern at 24.5 GPa. This clearly reveals the semimetal to superconductor transition at around 6 GPa is related to the phase transition from *Cmcm* to *C*2/*m*. In the high pressure range of 30.9–55.0 GPa, the story seems to be more complicated. Considering the mixture of monoclinic (*C*2/*m*) and triclinic (*P*-1) phases, the refinement overall matches with the experimental pattern. However, the feature with sharp peaks seems to indicate the occurrence of a cubic symmetry phase. Based on our current observation, we cannot rule out the possibility of separation of body-centered cubic (*bcc*) Te or a substitutional alloy of $ZrTe_x$ phase in form of any cubic structure in this pressure range.

We further performed Raman scattering measurements under pressure, as shown in Fig. S4. $ZrTe_5$ crystal at ambient pressure occupies an orthorhombic *Cmcm* (D_{2h}^{17}, No. 63) form, where the Wyckoff positions are 4*c* for Zr, 4*c* for Te1, and 8*f* for Te2 and Te3 atoms (29). Group theory analysis predicts 18 Raman-active modes in $ZrTe_5$, but only 12 of them were experimentally observed previously, including B_{1g}, B_{2g}, B_{3g}, and A_g modes (35). In addition, no striking changes in the Raman spectra were observed when the temperature is across the peak temperature in the electrical resistance (36), indicating no structural phase transition (11). Fig. S4, *Inset*, shows the prominent four A_g modes between 100 and 200 cm^{-1} at ambient pressure, with the most intense peak at 180 cm^{-1}, which are consistent with previous reports (35–37). Note that these A_g modes are strongly related to the specific Te2 or Te3 atoms. Under external pressure above 0.6 GPa, the profile of spectra retains similar to that of ambient pressure, whereas the former three modes shift toward higher wavenumber except the mode A_g^4, as shown in Fig. S4. When the pressure approaches 7.5 GPa where the superconducting transition emerges in *R*–*T* curve, these modes cannot be detected within the system resolution. These data provide additional evidence of pressure-induced structural phase transition, which matches our theoretical structure predictions and XRD measurements.

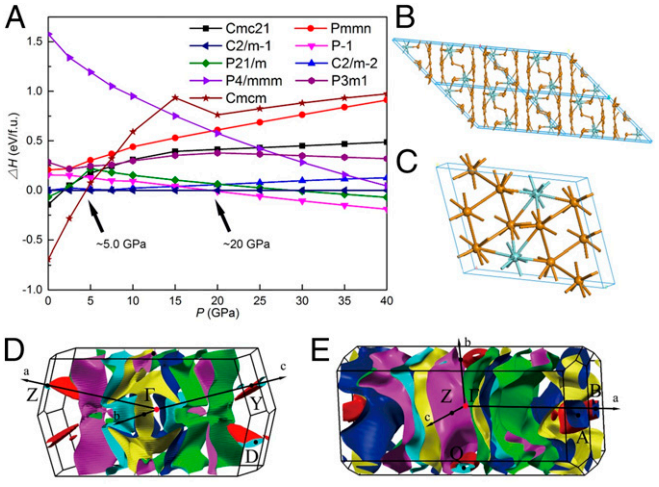

Fig. 4. Enthalpy calculation of possible stable phases and their atomic and electronic structures of $ZrTe_5$. Enthalpy vs. pressure for $ZrTe_5$ phases up to 40 GPa (*A*). Crystal structure of *C*2/*m* (*B*) and *P*-1 phase (*C*). The balls in cyan color and golden color represent Zr and Te atoms, respectively. (*D*) Fermi surfaces of *C*2/*m* structure at 10 GPa. (*E*) Fermi surfaces of *P*-1 structure at 30 GPa.

Discussions

Our calculations show that the pressure will change the crystal structure dramatically, and at around 6 GPa this compound becomes a metal. As shown in Fig. 4 *D* and *E* and Fig. S5, the Fermi surfaces of $ZrTe_5$ at high pressures are very complicated. There are five and seven bands crossing the Fermi level for *C*2/*m* and *P*-1 structure, respectively. A time-reversal-invariant topological superconductor requires odd-parity symmetry and the Fermi surface enclosing an odd number of time-reversal-invariant momenta (TRIM) (38). The states at Fermi surface are contributed to Zr-4*d* and Te-5*p*. Because these bands are spatially extended, the electronic correlation should be quite small due to the strong screening effect. Consequently, one can expect the superconductivity discovered in this work is mainly mediated by the electron–phonon interaction. Although the intrapocket phonon-mediated pairing, which may have singular behavior of the electron-phonon interaction at long wavelengths, can possess odd-parity symmetry (39). As shown in Fig. 4*D*, the Fermi surface does not enclose any TRIM. K-point D is not TRIM, although it is enclosed by the red–cyan sheet in Fig. 4*D*. Thus, this

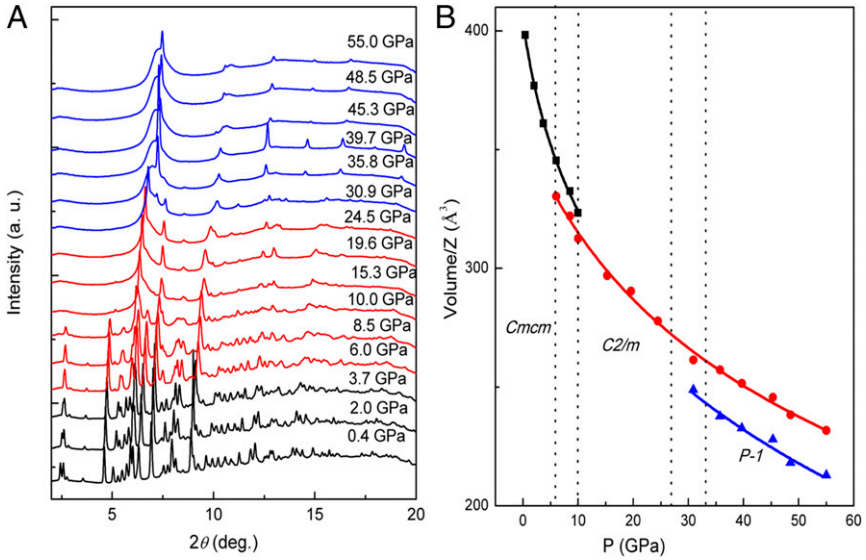

Fig. 5. High-pressure synchrotron X-ray diffraction patterns of $ZrTe_5$. (*A*) Representative diffraction patterns at high pressure from 0.4 to 55.0 GPa and room temperature. (*B*) Unit-cell volume per formula unit (*V*/*Z*) as a function of pressure. The solid square, circle, and upper trigonal denote the orthorhombic (*Cmcm*, Z = 4), monoclinic (*C*2/*m*, Z = 4), and triclinic (*P*-1, Z = 2) phase, respectively. The solid lines are the fitting results based on third-order Birch–Murnaghan equation of state. The vertical dot lines are guides for the eyes.

compound is unlikely the topological superconductor at least at low-pressure region (less than 10 GPa). We also perform band structure and Fermi surface calculations for high-pressure region. The Fermi surfaces become quite complicated as shown in Fig. 4e. There are three TRIM (A, B, Q) enclosed by two kinds of Fermi surfaces (denoted by red–cyan and red–blue, respectively.). As a result, the possibility of topological superconductivity at higher pressure cannot be excluded, which remains an open question.

From the phonon dispersions of *C*2/*m* and *P*-1 structures at 10 and 30 GPa, respectively, as shown in Fig. S6, both structures are confirmed to be dynamically stable under these pressures. This seems to agree with the experimental results that there are two superconducting phases under pressure. The superconducting properties of *C*2/*m* and *P*-1 structures are not calculated here due to the computational cost. But both of them are metallic phases, which can be seen from Figs. 4 *D* and *E*, and S5–S8.

In conclusion, by combining experimental and theoretical investigations, we demonstrated the pressure-induced superconductivity in a Dirac topological semimetal $ZrTe_5$ compound. The appearance of superconductivity at the critical pressure is accompanied by the complete suppression of the high temperature resistance anomaly around 128 K as well as a structural transition from *Cmcm* to *C*2/*m*. At pressures above 21.2 GPa, a second superconducting phase with *P*-1 structure manifests and coexists with the original *C*2/*m*. Although our theoretical study rules out the possibility of topological superconductivity at low pressure, at high pressure (above 20 GPa) the system has complicated Fermi surface and a second superconducting phase, thus deserving further study.

Materials and Methods

Single-Crystal Growth and Characterization. Single crystals of $ZrTe_5$ were grown via vapor transport method in a two-zone furnace with elements Zr (99.99%), Te (99.99%), and iodine (transport agent) (40). Structural and compositional characterizations of the crystals by X-ray diffraction, scanning and transmission electron microscopy, together with electron diffraction and energy dispersive X-ray spectroscopy studies confirm its high quality.

Experimental Details of High-Pressure Experiments. High pressures were generated with a screw-pressure-type diamond anvil cell (DAC) made of nonmagnetic Cu–Be alloy. The DAC was placed inside a homemade multifunctional measurement system (1.8–300 K, JANIS Research Company, Inc.; 0–9 T, Cryomagnetics, Inc.) with helium as the heat convection medium. Diamond anvils of 300-μm culets and T301 stainless-steel gasket covered with a mixture of epoxy and fine cubic boron nitride (cBN) powder were used for high-pressure transport measurements. A single crystal with dimension of $100 \times 30 \times 10$ μm^3 was loaded without pressure-transmitting medium in run 1, and another single crystal piece with $120 \times 90 \times 10$ μm^3 was loaded using Daphne 7373 oil as the pressure-transmitting medium in run 2. The four-probe method was applied in the *a*–*c* plane of single crystal in both runs. Platinum (Pt) foil with a thickness of 5 μm was used for the electrodes. The high-pressure *ac* magnetic susceptibility was measured using magnetic inductance technique. The 800-μm diamond culets and nonmagnetic Be–Cu gasket were used in run 3. Raman scattering measurements were performed at room temperature in a BeCu-type Diacell ST-DAC using a Horiba Jobin Yvon T64000 spectrometer equipped with a liquid nitrogen cooled charge-coupled device. The measurements were conducted in a pseudo backscattering configuration on freshly cleaved single crystal surfaces using 532-nm solid-state laser (torus 532, Laser Quantum) for excitation with a power below 0.1 mW to avoid sample damage and any heating effect. The back-scattered signal was collected in an unpolarized $Y(Z)\overline{Y}$ geometry through 50× objective and 1,800 g/mm grating. An integration time of 150 s was used. At room temperature, we inserted a flake (typically $100 \times 40 \times 10$ μm^3) cleaved parallel to the *a*–*c* plane and used Daphne 7373 oil as the pressure-transmitting medium. The high-pressure powder X-ray diffraction was conducted at 16-BM-D station, at High Pressure Collaborative Access Team (HPCAT), the Advanced Photon Source, Argonne National Laboratory. A focused monochromatic X-ray beam (~5 μm in FWHM) with wavelength 0.3091 Å was used for the angle-dispersive diffraction. A Mar345 image plate was used to record 2D diffraction patterns. FIT2D (41) and GSAS (33) programs were used for data integration and structure refinement. Pressure was calibrated by using the ruby fluorescence shift at room temperature for all experiments (42).

Density Functional Calculations. Ab initio random structure searching (43, 44) was applied for crystal structure predictions. Enthalpy calculation was performed using projector augmented wave implemented in the Vienna ab initio simulation package (VASP) (45). Phonon dispersion was carried out using finite displacement method with VASP and PHONOPY code (46). We used the Perdew–Burke–Ernzerhof generalized gradient approximation exchange-correlation density functional (47). The Brillouin zone was sampled with a Monkhorst–Pack **k**-mesh with a spacing of 0.03 Å^{-1}, and a $2 \times 2 \times 2$ supercell was chosen for phonon calculation. The plane wave cutoff was 288 eV, and structure relaxation was carried out until all of the atomic forces on each ion was less than 0.005 eV/Å. Electronic structures were carried out by using full-potential linearized augmented plane-wave method implemented in the WIEN2k package (48). $63 \times 19 \times 63$ and $63 \times 28 \times 22$ **k**-mesh were used to sample the Brillouin zone for Fermi surface calculation of the structure under 10 and 30 GPa, respectively. Spin-orbit coupling for all elements was taken into account by a second-variation method.

ACKNOWLEDGMENTS. This research was financially supported by the National Key Projects for Basic Research of China (Grants 2011CBA00111 and 2015CB921202), the National Natural Science Foundation of China (Grants U1530402, U1332139, U1332143, U1432251, 11574323, 11204312, 11374137, 11374302, 51372112, 11525417, and 11574133), Natural Science Foundation of Jiangsu province (BK20150012), and the Fundamental Research Funds for the Central Universities. W.Y. and H.-k.M. acknowledge the financial support from DOE-BES X-ray Scattering Core Program under Grant DE-FG02-99ER45775. Part of the calculations was performed on the supercomputer in the High Performance Computing Center of Nanjing University. High Pressure Collaborative Access Team (HPCAT) operations are supported by Department of Energy-National Nuclear Security Administration (DOE-NNSA) under Award DE-NA0001974 and Department of Energy-Basic Energy Science (DOE-BES) under Award DE-FG02-99ER45775, with partial instrumentation funding by National Science Foundation (NSF). Advanced Photon Source (APS) is supported by DOE-BES, under Contract DE-AC02-06CH11357.

1. Fu L, Kane CL, Mele EJ (2007) Topological insulators in three dimensions. *Phys Rev Lett* 98(10):106803.
2. Hasan MZ, Kane CL (2010) Topological insulators. *Rev Mod Phys* 82(4):3045–3067.
3. Qi X-L, Zhang S-C (2011) Topological insulators and superconductors. *Rev Mod Phys* 83(4):1057–1110.
4. Young SM, et al. (2012) Dirac semimetal in three dimensions. *Phys Rev Lett* 108(14): 140405.
5. Wan X, Turner AM, Vishwanath A, Savrasov SY (2011) Topological semimetal and Fermi-arc surface states in the electronic structure of pyrochlore iridates. *Phys Rev B* 83(20):205101.
6. Wan X, Vishwanath A, Savrasov SY (2012) Computational design of axion insulators based on 5*d* spinel compounds. *Phys Rev Lett* 108(14):146601.
7. Burkov AA, Balents L (2011) Weyl semimetal in a topological insulator multilayer. *Phys Rev Lett* 107(12):127205.
8. Jones TE, Fuller WW, Wieting TJ, Levy F (1982) Thermoelectric power of $HfTe_5$ and $ZrTe_5$. *Solid State Commun* 42(11):793–798.
9. Lowhorn ND, Tritt TM, Abbott EE, Kolis JW (2006) Enhancement of the power factor of the transition metal pentatelluride $HfTe_5$ by rare-earth doping. *Appl Phys Lett* 88(2):022101.
10. Okada S, Sambongi T, Ido M (1980) Giant resistivity anomaly in $ZrTe_5$. *J Phys Soc Jpn* 49(2):839–840.
11. Skelton EF, et al. (1982) Giant resistivity and X-ray diffraction anomalies in low-dimensional $ZrTe_5$ and $HfTe_5$. *Solid State Commun* 42(1):1–3.
12. Tritt TM, et al. (1999) Large enhancement of the resistive anomaly in the pentatelluride materials $HfTe_5$ and $ZrTe_5$ with applied magnetic field. *Phys Rev B* 60(11): 7816–7819.
13. Weng H, Dai X, Fang Z (2014) Transition-metal pentatelluride $ZrTe_5$ and $HfTe_5$: A paradigm for large-gap quantum spin hall insulators. *Phys Rev X* 4(1):011002.
14. Behrends J, Grushin AG, Ojanen T, Bardarson JH (2015) Visualizing the chiral anomaly in Dirac and Weyl semimetals with photoemission spectroscopy. *arXiv:150304329*.
15. Li Q, et al. (2014) Observation of the chiral magnetic effect in $ZrTe_5$. *arXiv:14126543*.
16. Chen RY, et al. (2015) Optical spectroscopy study of the three-dimensional Dirac semimetal $ZrTe_5$. *Phys Rev B* 92(7):075107.
17. Chen RY, et al. (2015) Magnetoinfrared spectroscopy of Landau levels and Zeeman splitting of three-dimensional massless Dirac fermions in $ZrTe_5$. *Phys Rev Lett* 115(17): 176404.
18. Wang Z, et al. (2012) Dirac semimetal and topological phase transitions in A_3Bi (A = Na, K, Rb). *Phys Rev B* 85(19):195320.
19. Liu ZK, et al. (2014) Discovery of a three-dimensional topological Dirac semimetal, Na_3Bi. *Science* 343(6173):864–867.
20. Xu S-Y, et al. (2015) Observation of Fermi arc surface states in a topological metal. *Science* 347(6219):294–298.
21. Wang Z, Weng H, Wu Q, Dai X, Fang Z (2013) Three-dimensional Dirac semimetal and quantum transport in Cd_3As_2. *Phys Rev B* 88(12):125427.
22. Borisenko S, et al. (2014) Experimental realization of a three-dimensional Dirac semimetal. *Phys Rev Lett* 113(2):027603.
23. Liu ZK, et al. (2014) A stable three-dimensional topological Dirac semimetal Cd_3As_2. *Nat Mater* 13(7):677–681.
24. Liang T, et al. (2015) Ultrahigh mobility and giant magnetoresistance in the Dirac semimetal Cd_3As_2. *Nat Mater* 14(3):280–284.
25. He LP, et al. (2014) Quantum transport evidence for the three-dimensional Dirac semimetal phase in Cd_3As_2. *Phys Rev Lett* 113(24):246402.
26. Zhang JL, et al. (2011) Pressure-induced superconductivity in topological parent compound Bi_2Te_3. *Proc Natl Acad Sci USA* 108(1):24–28.
27. Zhang C, et al. (2011) Phase diagram of a pressure-induced superconducting state and its relation to the Hall coefficient of Bi_2Te_3 single crystals. *Phys Rev B* 83(14):140504.
28. Kirshenbaum K, et al. (2013) Pressure-induced unconventional superconducting phase in the topological insulator Bi_2Se_3. *Phys Rev Lett* 111(8):087001.
29. Fjellvåg H, Kjekshus A (1986) Structural properties of $ZrTe_5$ and $HfTe_5$ as seen by powder diffraction. *Solid State Commun* 60(2):91–93.
30. McIlroy DN, et al. (2004) Observation of a semimetal-semiconductor phase transition in the intermetallic $ZrTe_5$. *J Phys Condens Matter* 16(30):L359.
31. Werthamer NR, Helfand E, Hohenberg PC (1966) Temperature and purity dependence of the superconducting critical field, H_{c2}. III. Electron spin and spin-orbit effects. *Phys Rev* 147(1):295–302.
32. Pavlosiuk O, Kaczorowski D, Wiśniewski P (2015) Shubnikov-de Haas oscillations, weak antilocalization effect and large linear magnetoresistance in the putative topological superconductor LuPdBi. *Sci Rep* 5:9158.
33. Larsen AC, Von Dreele RB (2000) General Structure Analysis System (GSAS). *Los Alamos National Laboratory Report LAUR*:86-748.
34. Birch F (1947) Finite elastic strain of cubic crystals. *Phys Rev* 71(11):809–824.
35. Landa G, Zwick A, Carles R, Renucci MA, Kjekshus A (1984) Lattice dynamics of the transition metal pentatellurides $ZrTe_5$ and $HfTe_5$. *Solid State Commun* 50(4):297–302.
36. Landa G, Zwick A, Carles R, Renucci MA, Kjekshus A (1984) Lacking Raman spectroscopic evidence for a structural phase transition in ZrTe5 at 141 K. *Solid State Commun* 49(11):1095–1098.
37. McGuire K, Lowhorn ND, Tritt TM, Rao AM (2002) Raman scattering in doped transition metal pentatellurides. *J Appl Phys* 92(5):2524–2527.
38. Fu L, Berg E (2010) Odd-parity topological superconductors: Theory and application to $Cu_xBi_2Se_3$. *Phys Rev Lett* 105(9):097001.
39. Wan X, Savrasov SY (2014) Turning a band insulator into an exotic superconductor. *Nat Commun* 5:4144.
40. Kamm GN, Gillespie DJ, Ehrlich AC, Wieting TJ, Levy F (1985) Fermi surface, effective masses, and Dingle temperatures of $ZrTe_5$ as derived from the Shubnikov-de Haas effect. *Phys Rev B Condens Matter* 31(12):7617–7623.
41. Hammersley AP, Svensson SO, Hanand M, Fitch AN, Hausermann D (1996) Two-dimensional detector software: From real detector to idealised image or two-theta scan. *High Press Res* 14(4-6):235–248.
42. Mao HK, Xu J, Bell PM (1986) Calibration of the ruby pressure gauge to 800 kbar under quasi-hydrostatic conditions. *J Geophys Res* 91(B5):4673–4676.
43. Pickard CJ, Needs RJ (2006) High-pressure phases of silane. *Phys Rev Lett* 97(4):045504.
44. Pickard CJ, Needs RJ (2011) *Ab initio* random structure searching. *J Phys Condens Matter* 23(5):053201.
45. Kresse G, Furthmüller J (1996) Efficiency of ab-initio total energy calculations for metals and semiconductors using a plane-wave basis set. *Comput Mater Sci* 6(1): 15–50.
46. Togo A, Oba F, Tanaka I (2008) First-principles calculations of the ferroelastic transition between rutile-type and $CaCl_2$-type SiO_2 at high pressures. *Phys Rev B* 78(13): 134106.
47. Perdew JP, Burke K, Ernzerhof M (1996) Generalized gradient approximation made simple. *Phys Rev Lett* 77(18):3865–3868.
48. Blaha P, Schwarz K, Madsen G, Kvasicka D, Luitz J (2001) *WIEN2k, An Augmented Plane Wave Plus Local Orbitals Program for Calculating Crystal Properties* (TU Vienna, Vienna, Austria).